

Centre Shift of the Raman Scattered He II λ 4850 in the Symbiotic Star V1016 Cygni

Yang-Chan Jung ^{*} and Hee-Won Lee [†]

Department of Astronomy and Space Science

Astrophysical Research Center for the Structure and Evolution of the Cosmos

Sejong University, Seoul, 143-747, Korea

Accepted 1988 December 15. Received 1988 December 14; in original form 1988 October 11

ABSTRACT

We present our spectroscopic data around H β of the symbiotic star V1016 Cyg obtained with the Bohyunsan Echelle Spectrograph, in order to secure the broad emission feature at around 4850 Å, which is formed through Raman scattering of He II λ 972. The total cross section around Ly γ is approximately given by $\sigma(\lambda) \simeq 1.7 \times 10^{-28} [\lambda_{Ly\gamma} / (\lambda - \lambda_{Ly\gamma})]^2 \text{ cm}^2$, with $\lambda_{Ly\gamma}$ being the line centre wavelength of Ly γ . We find a centre shift redward by an amount $\Delta\lambda = +0.64 \text{ \AA}$ in the Raman scattered He II λ 4850. This redward centre shift is exactly analogous to the effect for the Raman scattered He II λ 6545 blueward of H α discussed in our previous study. We compute the branching ratios of Raman scattering into the level 2s and levels 3s, and 3d, which are subsequently incorporated in our Monte Carlo code. Using this code, we present the centre shift of the 4850 feature as a function of the neutral hydrogen column density in the scattering region. Assuming that He II λ 972 emission is characterized by a single Gaussian profile, the redward peak shift observed in the Raman scattered He II 4850 feature corresponds to the neutral column density $N_{HI} = 1.2 \times 10^{21} \text{ cm}^{-2}$. Assuming that the covering factor ~ 0.1 of the scattering region with respect to the He II emission region and adopting a simple spherical stellar wind model, we may place an upper bound $\dot{M} \leq 3.6 \times 10^{-7} M_{\odot} \text{ yr}^{-1}$ for the mass loss rate of the giant component of V1016 Cyg. Our estimate can be severely affected by the kinematics of the scattering and He II emission regions and the exact atomic physics, about which brief discussions are presented.

Key words: scattering — radiative transfer — binaries: symbiotic — mass-loss — individual V1016 Cyg

1 INTRODUCTION

Symbiotic stars, believed to be a binary system of a giant and a hot white dwarf, are important objects for studying mass loss processes occurring in the late stage of stellar evolution (e.g. Kenyon 1986). A thick neutral hydrogen region formed around the giant component as a result of the mass loss is illuminated by strong UV radiation originating from the hot white dwarf component. Schmid (1989) identified the broad emission features around 6825 Å and 7088 Å found in more than half of the symbiotic stars by suggesting that they are formed via Raman scattering of the resonance doublet O VI 1032, 1038 by atomic hydrogen. Simultaneous observations in the far UV regions and many spectropolarimetric

observations strongly support this identification (e.g. Birriel, Espey & Schulte-Ladbeck 1998, 2000, Schmid & Schild 1994, Harries & Howarth 1996).

Raman scattering also appears to operate in the formation of H α wings that have been observed in most symbiotic stars and in a number of young planetary nebulae (Nussbaumer, Schmid & Vogel 1989, Lee 2000, Lee & Hyung 2000, Arrieta & Torres-Peimbert 2003). The H α profiles in the far wing regions are well fitted by $f_{\lambda} \propto \Delta\lambda^{-2} = (\lambda - \lambda_{H\alpha})^{-2}$, which delineates approximately the Raman scattering cross section, where $\lambda_{H\alpha}$ is the line centre wavelength of H α . He II $n \rightarrow 2$ emission lines arising from states with even principal quantum numbers have wavelengths only a little bit shorter than those of the H I Lyman series lines. These He II emission lines can be Raman scattered to form broad features blueward of the Balmer series lines.

We expect that the strongest Raman scattered He II

^{*} E-mail: ycjung@arcsec.sejong.ac.kr

[†] E-mail: hwlee@sejong.ac.kr

feature is formed at around 6545 Å blueward of H α , which is formed through Raman scattering of He II λ 1025. This feature was found in the spectra of the symbiotic stars RR Tel, He 2-106 and V1016 Cyg (Lee, Kang & Byun 2001, Lee et al. 2003). Another broad feature is formed at around 4850 Å, which is the Raman scattered feature of He II λ 972. This feature was reported in spectra of the symbiotic stars RR Tel (Van Groningen 1993) and V1016 Cyg (Birriel 2003). It is quite notable that the young planetary nebula NGC 7027 also exhibits this 4850 broad feature (Péquignot et al. 1997).

Raman scattered He II lines can be used as a powerful diagnostic of the mass loss processes in symbiotic stars, because the mass loss rate can be calculated by inferring the optical depth structures and the covering factor of the scattering region with respect to the UV emission region around the white dwarf. However, the flux of a Raman scattered He II feature is mainly determined by the product of the optical depth and the covering factor, which is a big barrier for the exact estimate of the mass loss rate.

In the previous theoretical study by Jung & Lee (2004, hereafter JL04), they showed that the Raman scattered He II λ 6545 should exhibit a redward centre shift by a significant amount depending on the H I column density of the scattering region around the giant in the absence of the relative motion between the scattering region and the emission region, which will lift the degeneracy of the optical depth and the covering factor. However, Raman scattered He II 6545 is usually blended with the forbidden line [N II] λ 6548, making it very hard to determine the exact peak location. This difficulty may be avoided when we use the Raman scattered He II 4850, which should be much weaker than the 6545 feature but be much easier to locate the peak wavelength.

UV radiation around Ly γ may have four scattering channels depending on the final state of the scattering atom, which can be one of 1s, 2s, 3s and 3d. When scattering occurs into either 3s or 3d level, energy conservation leads to the wavelength of the scattered radiation $\lambda_{3s,3d} = (\lambda_{He II 972}^{-1} - \lambda_{Ly\beta}^{-1})^{-1} = 1.85 \mu$, where $\lambda_{He II 972}$ and $\lambda_{Ly\beta}$ are line centre wavelengths for He II λ 972 and Ly β . Therefore, in order to simulate the Raman scattered He II lines accurately, it is necessary to compute the branching ratios into 3s and 3d states. This calculation will also be useful for the future study of Raman scattered lines formed blueward of Paschen series lines.

In this paper, we present an optical spectrum around H β of the symbiotic star V1016 Cygni obtained with the 1.8 m Bohyunsan telescope and our Monte Carlo calculations of Raman scattering around Ly γ , in order to determine the neutral hydrogen column density of the scattering region around the giant component.

2 OBSERVATIONAL DATA

We observed V1016 Cyg on the night of 2003 December 16 with the Bohyunsan Optical Echelle Spectrograph equipped with a 2k \times 4k E2V CCD installed on the 1.8 m telescope at Mt. Bohyun. We used the 200 μ optical fiber that yields the spectroscopic resolution $R = 44,000$ and the exposure time was 3000 s. The data have been reduced following standard procedures using the IRAF packages. In Fig. 1, we show the

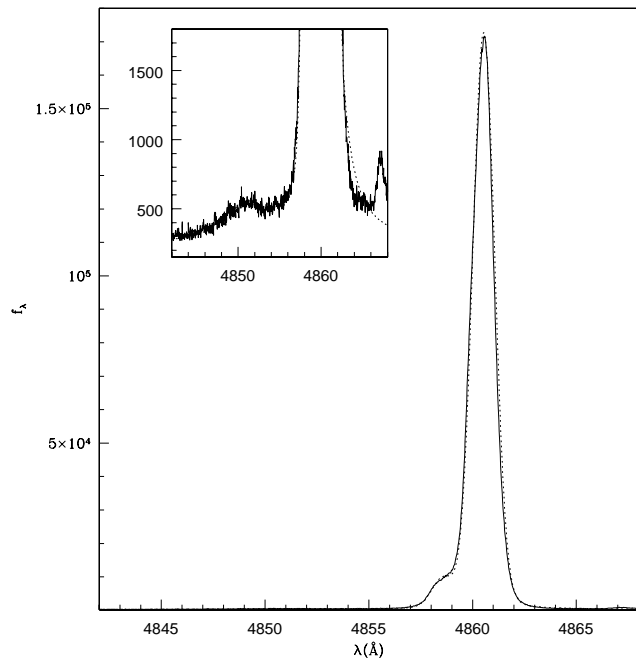


Figure 1. The optical spectrum around H β of V1016 Cyg obtained with the Bohyunsan Optical Echelle Spectrograph (BOES) installed on the 1.8 m telescope at Mt. Bohyun. The spectroscopic resolution is 44,000 and the exposure time was 3000 s. The thin solid lines represent our single Gaussian fits to the emission lines H β , He II λ 4861 and the Raman scattered He II λ 4850. From our Gaussian fitting, the Raman scattered He II λ 4850 is shifted redward by an amount $\Delta\lambda = +0.64$ Å with respect to the emission line center He II λ 4861.

part of our spectrum that contains H β . The solid line shows the observed spectrum, and in the inset we enhanced the part exhibiting the Raman scattered He II λ 4850 feature. In this figure, the vertical axis is shown in an arbitrary unit, which is sufficient for the purpose of this work.

We measure the relative shift from the emission lines He II λ 4861 and H β , where these emission lines are assumed to be isotropic in their emission region. This assumption may not be true in the accuracy required in this work. In the case of O VI λ 1032, 1038 doublet, it is known that their profiles and those of their Raman scattered 6825, 7088 features differ quite significantly (Schmid et al. 1999). The O VI doublet lines are strong resonance lines that are subject to various radiative transfer effects, whereas optical He II recombination lines are expected to be relatively free from such effects. This may be checked by monitoring the variations as a function of the orbital phases. In this work, we take the He II λ 4861 and H β as the local reference of velocity and measure the line centre shift of the Raman scattered He II λ 4850.

In Fig. 1, we applied single Gaussian fits to both He II λ 4861 and H β to locate their peak positions. The dotted lines show our fit, which we can barely notice in the figure. This implies that satisfactory fits are obtained for both emission lines. For He II λ 4861, the fitting function is $f_{He II} = f_1 e^{-[(\lambda - \lambda_1)/\Delta\lambda_1]^2}$ and for H β it is $f_{H\beta} = f_2 e^{-[(\lambda - \lambda_2)/\Delta\lambda_2]^2}$, where $f_1 = 165000$, $f_2 = 8200$, $\lambda_1 = 4860.54$ Å, $\lambda_2 = 4858.57$ Å and $\Delta\lambda_1 = \Delta\lambda_2 = 0.75$ Å.

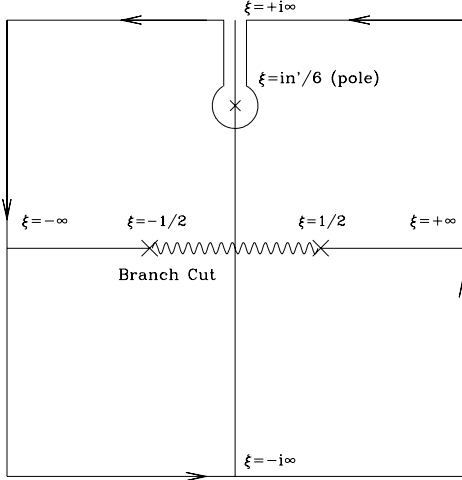


Figure 2. The contour C for the integral in Eq. 9. There is a branching cut on the real axis between $\xi = 1/2$ and $\xi = -1/2$. There is a pole at $\xi = in'/6$, at which residues are computed.

The 4850 feature is also fitted with a single Gaussian

$$f_{4850} = f_3 e^{-[(\lambda - \lambda_3)/\Delta\lambda_3]^2}, \quad (1)$$

where the least square method yields $\lambda_3 = 4850.63 \text{ \AA}$ and $\Delta\lambda_3 = 3.76 \text{ \AA}$. We note that the width broadening is in excellent agreement with the theoretical expectation

$$\Delta\lambda_3/\Delta\lambda_1 \simeq 4861/972 = 5.0. \quad (2)$$

Using the atomic data compiled by van Hoof, the centre wavelength λ_0 in vacuum of the Raman scattered He II λ 972 is

$$\lambda_0 = (\lambda_{He II 972}^{-1} - \lambda_\alpha^{-1})^{-1} = 4852.098 \text{ \AA}, \quad (3)$$

where the vacuum wavelength of Ly α is $\lambda_\alpha = 1215.67 \text{ \AA}$ and that for He II λ 972 is $\lambda_{He II 972} = 972.112 \text{ \AA}$. Considering the refractive index of air $n_{air} = 1.000279348$, the line centre of the 4850 feature appears at $\lambda_3^0 = 4850.743 \text{ \AA}$ in air. Noting that the line center of He II λ 4861 in our spectrum appears at $\lambda_{He II} = 4859.320 \text{ \AA}$, our spectrum of V1016 Cyg shows the redward centre shift $\Delta\lambda = +0.64 \text{ \AA}$ in the 4850 feature with respect to their emission region.

3 ATOMIC PHYSICS

We compute the matrix elements necessary for computation of the contribution to the scattering cross section of the levels $3s$ and $3d$. The contributions of the levels $1s$ and $2s$ have been presented in the literature (e.g. Saslow & Mills 1967, Sadegpour & Dalgarno 1992, Lee & Lee 1997).

According to Karzas & Latter (1961), the matrix ele-

ment for bound-bound state transition is given by

$$\begin{aligned} \tau_{nl}^{n'l-1} &= \int_0^\infty r R_{n'l-1}(r) R_{nl}(r) r^2 dr \\ &= \frac{2^{2l}}{(2l-1)!} \left[\frac{(n+l)!(n'+l-1)!}{(n-l-1)!(n'-l)!} \right]^{1/2} (nn')^{l+1} \\ &\times (n+n')^{-n-n'} (n-n')^{n-2-l} (n'-n)^{n'-l} \\ &\times \left\{ F(l-n+1, l-n', 2l, x_{n,n'}) \right. \\ &\left. - \left(\frac{n-n'}{n+n'} \right)^2 F(l-n-1, l-n', 2l, x_{n,n'}) \right\}, \quad (4) \end{aligned}$$

where $x_{n,n'} \equiv -4nn'/(n-n')^2$ and $F(\alpha, \beta, \gamma, x)$ is the hypergeometric function

$$F(\alpha, \beta, \gamma, x) \equiv 1 + \frac{\alpha\beta}{\gamma} \frac{x}{1!} + \frac{\alpha(\alpha+1)\beta(\beta+1)}{\gamma(\gamma+1)} \frac{x^2}{2!} + \dots \quad (5)$$

Here, $R_{nl}(r)$ is the radial wavefunction of a hydrogen atom, which can be expressed using a confluent geometric function F_1 by

$$\begin{aligned} R_{nl}(r) &= \frac{1}{(2l+1)!} \sqrt{\frac{(n+l)!}{(n-l-1)!2n}} \left(\frac{2Z}{n} \right)^{3/2} e^{-Zr/n} \\ &\left(\frac{2Zr}{n} \right) F_1(-(n-l-1), 2l+2; 2Zr/n), \quad (6) \end{aligned}$$

where $F_1(a, b, x) \equiv 1 + abx + [a(a+1)b(b+1)/2!]x^2 + \dots$.

By setting $n' = 3, l = 1$, a straightforward calculation leads to

$$\begin{aligned} \tau_{3s}^{np} &\equiv \langle 3s \parallel r \parallel np \rangle = \frac{1}{4} \left[\frac{(n+1)!3!}{(n-2)!(3-1)!} \right]^{1/2} \\ &\times \frac{(12n)^2(n-3)^{n+3-4}}{(n+3)^{n+3}} \\ &\times \left\{ F(-n+2, -2, 2, \frac{-12n}{(n-3)^2}) \right. \\ &\left. - \left(\frac{n-3}{n+3} \right)^2 F(-n, -2, 2, \frac{-12n}{(n-3)^2}) \right\} \\ &= 3^{3/2} 12^2 n^{7/2} \sqrt{n^2-1} (17n^2-27) \frac{(n-3)^{n-4}}{(n+3)^{n+4}}. \quad (7) \end{aligned}$$

By interchanging n and n' in Eq. (1) and letting $n' = 3, l = 2$, we obtain

$$\begin{aligned} \tau_{3d}^{np} &\equiv \langle 3d \parallel r \parallel np \rangle = \frac{1}{24} \left[\frac{(n+1)!5!}{(n-2)!0!} \right]^{1/2} \\ &\times \frac{(12n)^3(n-3)^{n-3}}{(n+3)^{n+3}} \\ &\times \left\{ F(0, -n+2, 4, \frac{-12n}{(n-3)^2}) \right. \\ &\left. - \left(\frac{n-3}{n+3} \right)^2 F(-2, -n+2, 4, \frac{-12n}{(n-3)^2}) \right\} \\ &= \frac{12^3 \sqrt{3}}{\sqrt{10}} n^{11/2} \sqrt{n^2-1} \frac{(n-3)^{n-4}}{(n+3)^{n+4}}. \quad (8) \end{aligned}$$

According to Bethe & Salpeter (1957) the wavefunction for the continuum states $n'p$ is given by the contour integral

$$R_{n'l=1} = \frac{[1+n'^2]^{1/2}}{\pi[1-e^{-2\pi n'}]^{1/2}} \frac{n'^2}{4r^2}$$

$$\times \int_C e^{-2ir\xi/n'} (\xi + \frac{1}{2})^{-in'-2} (\xi - \frac{1}{2})^{in'-2} d\xi, \quad (9)$$

where the contour C is depicted in Fig. 2.

The matrix element for a dipole operator between $3s$ and $n'p$ states is

$$\begin{aligned} \tau_{n'p}^{3s} &= \langle 3s|r|n'p \rangle \\ &= \frac{n'^{1/2}[1+n'^2]^{1/2}}{4\pi[1-e^{-2\pi n'}]} \int_C (\xi + 1/2)^{-in'-2} (\xi - 1/2)^{in'-2} d\xi \\ &\times \int_0^\infty dr r e^{-\frac{2i\xi r}{n'}} \frac{2}{3\sqrt{3}} e^{-r/3} \left(1 - \frac{2r}{3} + \frac{2r^2}{27}\right). \end{aligned} \quad (10)$$

Letting $\lambda = \frac{1}{3} + \frac{2i\xi}{n'}$ the radial integral becomes

$$\begin{aligned} I_1 &= \frac{2}{3\sqrt{3}} \int_0^\infty e^{-r(1/3+2i\xi/n')} \left(1 - \frac{2r}{3} + \frac{2r^2}{27}\right) dr \\ &= \frac{2}{3\sqrt{3}} \left[\frac{1}{\lambda^2} - \frac{4}{3\lambda^3} + \frac{4}{9\lambda^4} \right]. \end{aligned} \quad (11)$$

Using the residue theorem for the pole at $\xi = in'/6$, we compute the contour integral

$$\begin{aligned} I_2 &= \int_C d\xi (\xi + 1/2)^{-in'-2} (\xi - 1/2)^{in'-2} \\ &\times \left[\frac{1}{\lambda^2} - \frac{4}{3\lambda^3} + \frac{4}{9\lambda^4} \right] \\ &= \frac{6^5 \pi n'^3}{(n'^2 + 9)^4} (7n'^2 + 27) e^{-2n' \tan^{-1}(3/n')}. \end{aligned} \quad (12)$$

Substituting this result we have

$$\tau_{3s}^{n'p} = \frac{3^{3/2} 12^2 n'^{7/2} (1+n'^2)^{1/2} (7n'^2 + 27)}{(1-e^{-2\pi n'}) (n'^2 + 9)^4} e^{-2n' \tan^{-1}(3/n')}. \quad (13)$$

A similar procedure gives

$$\tau_{3d}^{n'p} = \frac{12^3}{\sqrt{10}} \frac{n'^{11/2} (1+n'^2)^{1/2}}{(1-e^{-2\pi n'}) (n'^2 + 9)^4} e^{-2n' \tan^{-1}(3/n')}. \quad (14)$$

In Fig. 3 we show the scattering cross sections and branching ratios as a function of the wavelength of UV radiation around Ly γ . In the upper panel we show the total scattering cross section σ_T by a thick solid line, the cross section σ_{2s} for Raman scattering into the $2s$ level by a dot-dashed line, and the cross section σ_{3s3d} for Raman scattering into the $3s-3d$ levels by a dashed line.

Also in the upper panel, the dotted line shows a Lorentzian fit to the total scattering cross section, which is given by

$$\sigma(\lambda) = \sigma_0 \left(\frac{\lambda_{Ly\gamma}}{\lambda - \lambda_{Ly\gamma}} \right)^2. \quad (15)$$

Here, $\lambda_{Ly\gamma}$ is the line centre wavelength for the Ly γ transition. With this fit, we set $\sigma_0 = 0.17 \times 10^{-27} \text{ cm}^2$. As is for the case of Ly α shown by Lee (2003), the total cross section is also asymmetrical with respect to the Ly γ line center, which is noticeable in this fit. At the line centre $\lambda = 972.112 \text{ \AA}$ of He II $\lambda 972$, the total scattering cross section is

$$\sigma_{tot, He II 972} = 0.91 \times 10^{-21} \text{ cm}^2. \quad (16)$$

This may be compared with the total scattering cross section for He II $\lambda 1025$, which is $\sigma_{tot, He II 1025} = 6.2 \times 10^{-21} \text{ cm}^2$. From this computation, we may regard the Raman scattered He II $\lambda 6545$ as a probe for neutral regions with $N_{HI} \sim$

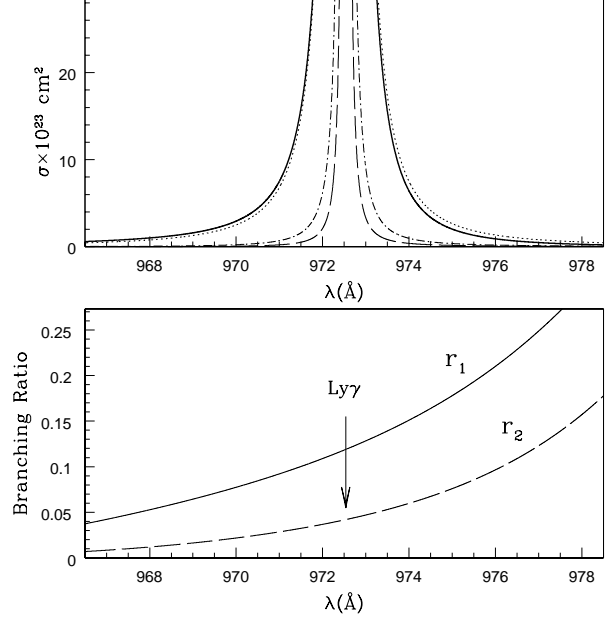


Figure 3. The scattering cross sections and branching ratios of UV radiation around Ly γ by atomic hydrogen. In the upper panel, the solid line shows the total scattering cross section, the dot-dashed line represents the scattering cross section into the level $2s$ (for He II $\lambda 4850$) and the dashed line represents the sum of the scattering cross sections into the levels $3s$ and $3d$. Also in the upper panel, the dotted line shows a Lorentzian fit to the total scattering cross section by the formula $\sigma_0[\lambda_{Ly\gamma}/(\lambda - \lambda_{Ly\gamma})]^{-2}$, where $\lambda_{Ly\gamma}$ is the line centre wavelength of Ly γ and $\sigma_0 = 1.7 \times 10^{-28} \text{ cm}^2$. In the lower panel, we show the branching ratio r_1 of Raman scattering into the level $2s$ by a solid line, and the branching ratio r_2 into the levels $3s$ and $3d$ by a dashed line.

10^{20} cm^{-2} and the Raman scattered He II 4850 is formed mainly in regions with $N_{HI} \geq 10^{21} \text{ cm}^{-2}$.

In the lower panel of Fig. 3, we show the branching ratios $r_1 = \sigma_{2s}/\sigma_T$, $r_2 = \sigma_{3s3d}/\sigma_T$ for Raman scattering into the $2s$ level and the $3s-3d$ levels by a solid line and a dashed line, respectively. It is quite notable that the branching ratio into the level $2s$ is about 3 times larger than the sum of the branching ratios into $3s$ and $3d$ near He II $\lambda 972$. Raman scattering into levels $3s$ and $3d$ will leave a broad feature at $\lambda = 1.85\mu$ blueward of Pa α . According to this calculation, it is expected that the $\lambda = 1.85\mu$ feature will be constituted by a smaller number of photons by a factor of $1/3$ than those in the Raman scattered He II $\lambda 4850$. At around $\lambda = 985 \text{ \AA}$ the total cross section is dominated by the scattering channel into the levels $n = 3$, for which, however, the scattering cross section is very small. Near the line center of Ly β the branching ratio for the levels $n = 3$ becomes negligibly small due to the decrease of the phase space volume and becomes zero redward of Ly β , which is forbidden by energy conservation.

4 CALCULATIONS

4.1 Monte Carlo Procedures

The same Monte Carlo code used in the previous study by JL04 is slightly modified with an addition of subroutines for those scattering channels into $3s$ and $3d$ levels. The code incorporates the channel for Rayleigh scattering as well as the two channels for Raman scattering. Therefore, we followed faithfully paths of He II photons suffering several Rayleigh scatterings followed by a Raman scattering in the H I region. However, no dust effect is considered in the current work.

As in JL04, considering the fact that He II 6560, He II 4686 emission lines are well fitted by a single Gaussian

$$f_\lambda = f_0 \exp[-(\lambda - \lambda_0)^2 / \Delta\lambda^2], \quad (17)$$

with the velocity width $\Delta\lambda/\lambda_0 = (23 \text{ km s}^{-1}/c)$. We use the same single Gaussian for the incident radiation. Since we are only concerned with the exact location of the central peak, we do not require the exact equivalent width of the He II λ 972 line and set it to be 0.1\AA .

When the scattering region is optically thin, the strength of the Raman scattered feature is mainly determined by the product of the incident radiation flux and the scattering cross section. The He II λ 972 incident line radiation has a profile that is symmetric with respect to its line center, whereas the scattering cross section is highly inclined toward the line center of Ly γ , which is located redward of He II 972. This induces a redward shift of the peak in the Raman scattered He II λ 4850, as is explained for the Raman scattered He II λ 6545 in JL04. We illustrate this situation in Fig. 4, where the dotted line shows the Raman scattering cross section into the level $2s$ relevant to the formation of the 4850 feature. In this figure, the dashed line shows the sum of the Raman scattering cross sections into the levels $3s$ and $3d$, which is slightly larger than the quantity represented by the dotted line in this region.

Due to the multiple scattering effect that is important for a very optically thick scattering region, the peak shift will decrease as N_{HI} increases, and therefore a Monte Carlo technique is useful to obtain a reliable quantitative relation.

4.2 Results

4.2.1 Balmer and Paschen Wings

In Fig. 5, we show typical Raman scattered He II features formed in the blue region of H α , H β and Pa α , where we set $N_{HI} = 3 \times 10^{20} \text{ cm}^{-2}$. The formation of the 6545 feature was studied intensively by JL04, and here it was reproduced for comparisons with those obtained from Raman scattering of UV radiation around Ly γ . The vertical axis shows the number of photons obtained from the Monte Carlo simulations for 5×10^4 continuum photons per wavelength interval of $\Delta\lambda = 0.00125 \text{ \AA}$ in the UV rest frame around Ly γ .

We normalize the horizontal scale by the velocity $c(\Delta\lambda_R/\lambda_R)$ from the line centres of Raman scattering, where $\lambda_R = 6563, 4861, \text{ and } 18751 \text{ \AA}$ respectively. With this normalization, the flux density at λ_R in the Raman scattered features is diluted by the factor $\lambda_R/\lambda_{Ly\gamma}$.

Far from the line centres of Balmer lines and Pa α , the Rayleigh and Raman scattering optical depth is quite small, and the Raman wings exhibit profiles that are proportional

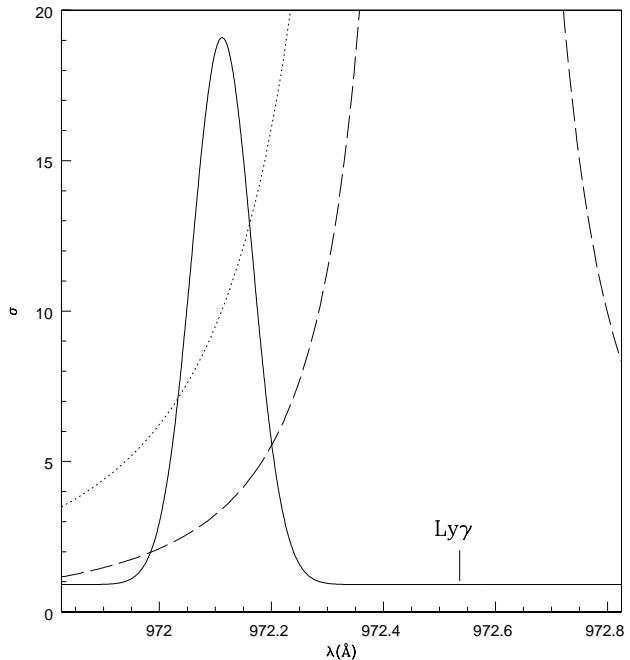


Figure 4. The Raman scattering cross sections overplotted to the He II 972 emission line given by a single Gaussian with $\Delta\lambda = 0.076 \text{ \AA}$. The dotted line shows the cross section of the Raman scattering into the $2s$ level, and the dashed line shows the sum of the cross sections for the Raman scattering into the $3s$ and $3d$ levels. Note that the cross section increases steeply toward the Ly γ line center, which will affect the center location of the Raman scattered He II 4850 feature.

to the total scattering cross section multiplied by the corresponding branching ratio. It is notable that the sum of the branching ratios for levels $3s$ and $3d$ is smaller by a factor $1/3$ than the branching ratio for level $2s$, and therefore our simulations show that the Raman scattered feature blueward of Pa α is weaker by the similar factor than the feature blueward of H β .

Near the line centres of Balmer lines and Pa α , the total scattering optical depth is quite large and the Raman conversion efficiency no longer increases toward the line center. Instead, almost all incident Ly γ photons may be singly scattered at the surface of the scattering region by a Rayleigh or Raman process, or may suffer a few Rayleigh scatterings followed by Raman scattering or final Rayleigh scattering before escape, which leads to nearly constant Raman conversion efficiencies into around H β and Pa α . More quantitatively, according to our Monte Carlo results, about 36 percent of incident photons very near Ly γ line center are converted and redistributed around H β and 13 percent of them are redistributed around Pa α .

It is also quite notable that the Raman feature blueward of Pa α appears 4 times further away from the centre of Pa α than the 4850 feature is away from the H β centre. This is attributed to the difference in the ratio λ_o/λ_i of the wavelengths of the Raman scattered radiation and incident UV radiation.

From this figure, we infer that the wings around H β and Pa α are very weak compared with those around H α , unless

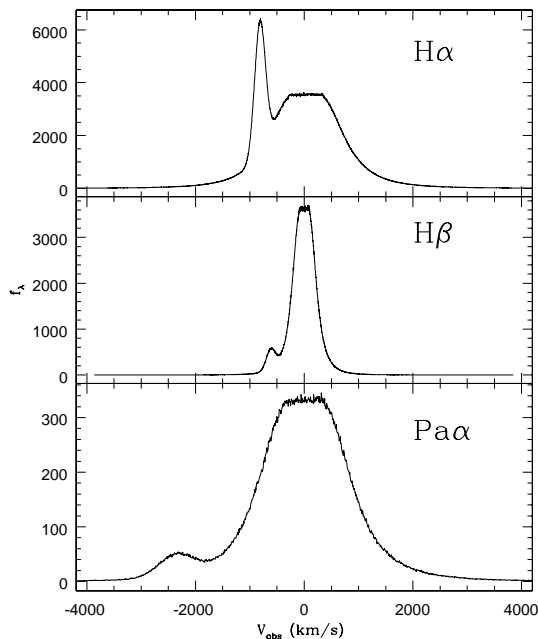


Figure 5. Typical Raman scattered He II features formed blueward of H α , H β and Pa α . The H I column density of the scattering region is assumed to be $N_{HI} = 3 \times 10^{20} \text{ cm}^{-2}$. We normalize the horizontal scale by the velocity $c(\Delta\lambda_R/\lambda_R)$ from the line centres of Raman scattering, where $\lambda_R = 6563, 4861,$ and 18751 \AA respectively. Note that with this normalization the flux density is diluted by the factor $\lambda_R/\lambda_{Ly\gamma}$. The vertical axis shows the number of photons obtained from the Monte Carlo simulations for 5×10^4 continuum photons per wavelength interval of $\Delta\lambda = 0.00125 \text{ \AA}$ in the UV rest frame around Ly γ .

the continuum around Ly γ is unrealistically stronger than that around Ly β . The relative strengths of H α and H β wings may be useful in distinguishing those wings that are formed from other mechanisms including Thomson scattering.

4.2.2 H β wings and the Raman Scattered He II $\lambda 4850$

In Fig. 6 we show H β wings and the Raman scattered He II $\lambda 4850$ feature for 4 values of N_{HI} . The extent of H β wings increases as N_{HI} increases and the wing profile is approximately by $(\lambda - \lambda_{H\beta})^{-2}$. A saturation behaviour is seen near the line center of H β at which the Raman scattering optical depth becomes larger than unity. The strength of the Raman scattered He II $\lambda 4850$ also increases as N_{HI} .

In Fig. 7, in order to illustrate the centre shift phenomenon clearly, we overplot profiles of the Raman scattered He II $\lambda 4850$ obtained for various N_{HI} as we increase N_{HI} starting from $N_{HI} = 2 \times 10^{20} \text{ cm}^{-2}$ by a step of $\Delta N_{HI} = 4 \times 10^{20} \text{ cm}^{-2}$. Here, we use the same incident radiation as in Fig. 6. Because the strength of the 4850 feature increases as N_{HI} , stronger profiles correspond to higher N_{HI} . It is immediately seen in this figure that the amount of centre shift decreases as N_{HI} .

In Fig. 8, we show the centre shift of He II $\lambda 4850$ feature as a function of N_{HI} , treating the scattering region as a plane-parallel slab characterized by a single column den-

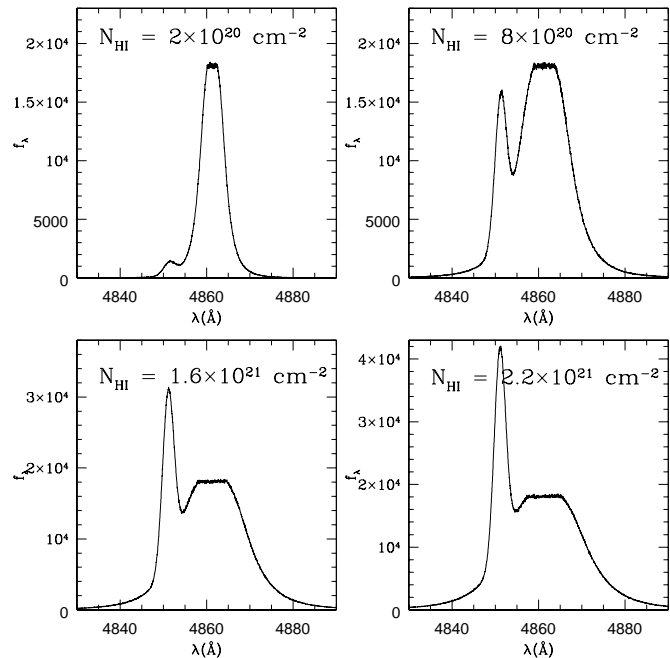


Figure 6. The Raman scattered He II $\lambda 4850$ feature formed in neutral scattering regions with various H I column densities. The strength and the centre shift of the He II $\lambda 4850$ feature exhibit similar behaviours to those of the He II $\lambda 6545$ feature discussed by JL04. The incident radiation is prepared in the same way as in Fig. 5 and the vertical axis has the same meaning as in Fig. 5.

sity. As is emphasized earlier, we assume that the scattering region is static with respect to the emission region and measure the relative shift from the He II $\lambda 4861$. There exist fluctuations in the result shown in Fig. 8, which is indicative of the statistical nature of the Monte Carlo calculation. We provide a simple fit to our data, which is given by

$$(\Delta\lambda/1 \text{ \AA}) = 0.73 - 0.015x + 0.83(0.8 + x)^{-0.9}, \quad (18)$$

where $x = N_{HI}/10^{20} \text{ cm}^{-2}$ is the H I column density in units of 10^{20} cm^{-2} .

The behaviour of the centre shift for He II $\lambda 4850$ as a function of N_{HI} is almost similar to that for He II $\lambda 6545$. For $N_{HI} \geq 10^{19} \text{ cm}^{-2}$, the amount of centre shift decreases as N_{HI} increases. We omit the description of our results, which can be found for Raman scattered He II $\lambda 6545$ in JL04. According to our Monte Carlo calculation, the observed centre shift by an amount 0.64 \AA is obtained when $N_{HI} = 1.2 \times 10^{21} \text{ cm}^{-2}$. It is particularly notable that the slope of the centre shift as a function of N_{HI} is small for high column densities, so that the accurate determination of N_{HI} may be significantly affected by the relative motion between the He II emission region and the neutral scattering region.

4.3 Estimate of the Mass Loss Rate

Assuming a spherical stellar wind from the giant component in V1016 Cyg, we may set the hydrogen number density

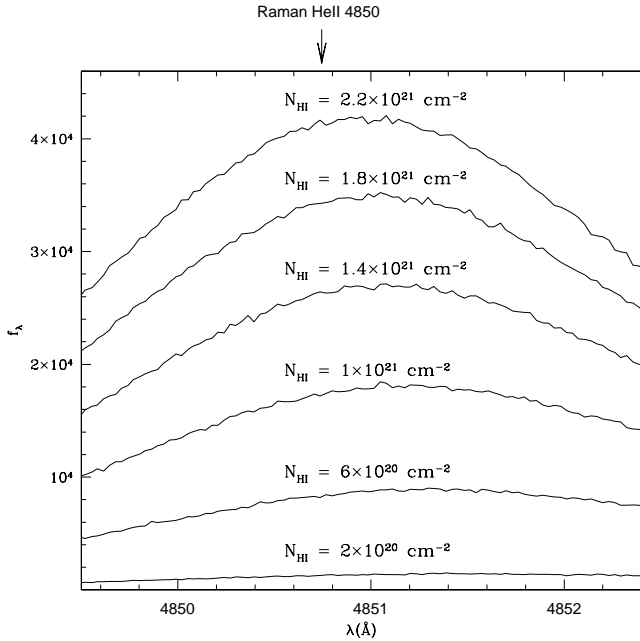


Figure 7. The profiles of He II λ 4850 feature obtained for various column densities overplotted. The incident He II λ 972 is assumed to be given by a single Gaussian with a width $\Delta\lambda = 0.076 \text{ \AA}$ and the neutral scattering region is a plane-parallel slab characterized by a single column density N_{HI} . N_{HI} is increased from $N_{HI} = 2 \times 10^{20} \text{ cm}^{-2}$ in steps of $\Delta N_{HI} = 4 \times 10^{20} \text{ cm}^{-2}$.

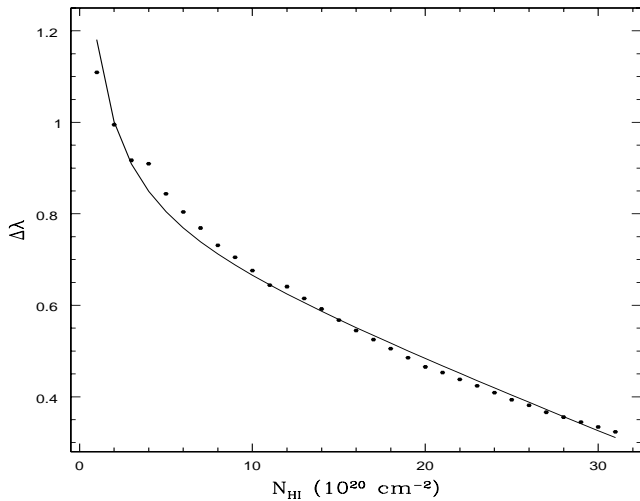


Figure 8. The centre shift of He II λ 4850 feature as a function of N_{HI} . The incident He II λ 972 is assumed to be given by a single Gaussian with a width $\Delta\lambda = 0.076 \text{ \AA}$ and the neutral scattering region is a plane-parallel slab characterized by a single column density N_{HI} . We give a simple fit to our data by $(\Delta\lambda/1 \text{ \AA}) = 0.73 - 0.015x + 0.83(0.8 + x)^{-0.9}$, where $x = N_{HI}/10^{20} \text{ cm}^{-2}$ is the H I column density in units of 10^{20} cm^{-2} .

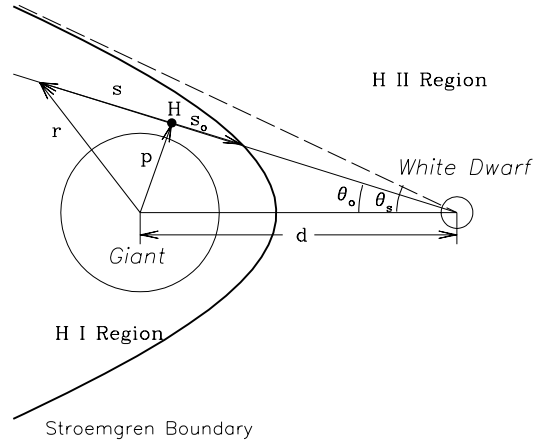


Figure 9. A schematic diagram for the scattering geometry in V1016 Cyg. Depending on the density structure around the giant and the strength of the UV radiation from the white dwarf, the Strömgren boundary is formed, which is defined as the loci of the ionization front dividing the H I region from H II region. The point H is the foot of the perpendicular to a sightline from the white dwarf with an impact parameter p making an angle θ_o with the axis connecting the giant and dwarf. The parameter s measures the distance from H to a given point along the sightline with a distance r from the giant so that $r^2 = s^2 + p^2$. By θ_s we denote the smallest angle of the line of sight from the white dwarf making with the axis connecting the giant and the white dwarf, for which no H I region can be reached.

$$n(r) = \frac{\dot{M}}{4\pi\mu m_p v_\infty r^2}, \quad (19)$$

where \dot{M} is the mass loss rate of the giant, m_p is the proton mass, μ is the mean molecular weight, and v_∞ is the terminal velocity of the slow stellar wind.

Depending on the density structure and the ionizing luminosity, the ionization structure will be determined (e.g. Taylor & Seaquist 1984). A schematic diagram for this situation is shown in Fig. 9, where d is the binary separation. In this figure, we denote the ionization front by the Strömgren boundary which separates the H I region around the giant from the H II region formed around the white dwarf. By θ_s we denote the smallest angle of the line of sight from the white dwarf making with the axis connecting the giant and the white dwarf, for which the H I region cannot be reached.

We consider a sightline from the white dwarf to the H I region. The point H is the foot of the perpendicular to this sightline from the white dwarf with an impact parameter p making an angle θ_o with the axis connecting the giant and dwarf. The parameter s measures the distance from H to a given point along the sightline with a distance r from the giant so that $r^2 = s^2 + p^2$. The H I column density for this sightline with the impact parameter p is given by

$$N(p) = \int_{-s_0}^{\infty} n(r) ds = \frac{\dot{M}}{4\pi\mu m_p v_\infty p} \left[\frac{\pi}{2} + \tan^{-1} \frac{s_0}{p} \right], \quad (20)$$

where s_0 is the distance from H to the Strömgren boundary.

Brocksopp et al. (2002) analysed optical and radio images of V1016 Cyg obtained with the Hubble Space Telescope and the Very Large Array (VLA). Adopting a distance of 2 kpc they suggest that the projected binary separation of V1016 Cyg is $d = 84 \pm 2$ AU. Previous works by other researchers provide smaller binary separations and shorter binary periods. For example, Schmid & Schild (2002) performed spectropolarimetry to investigate the variation of the polarization direction which is expected to vary due to the orbital motion. Based on their polarimetric method, they proposed that the binary period may exceed 100 years. Lee et al. (2003) investigated the strength of the 6545 feature in V1016 Cyg, and suggested the opening half angle $\theta_s \simeq 60^\circ$ adopting the distance estimate by Brocksopp et al. (2002).

We adopt $\mu = 1.4$ as suggested by Mürset & Nussbaumer (1994), $v_\infty = 10$ km s $^{-1}$. We choose a sightline from the white dwarf with θ_o just a little bit smaller than θ_s , for which $p \simeq d \sin \theta_s \simeq 73$ AU. We may identify the H I column density $N_{HI}^0 = 1.2 \times 10^{21}$ cm $^{-2}$ that yields the observed centre shift with that for this sightline. We note that the exact choice of s_o affects the final result by a factor of two. However, in the case where the Strömgren boundary is well approximated by a hyperbola as noted by Schmid (1995), we believe that s_o is not much greater than p . Here, we just neglect this term and set $N_{HI} \simeq \dot{M}/[8\mu m_p v_\infty p]$. From this consideration, we may obtain

$$\dot{M} = 3.6 \times 10^{-7} M_\odot \text{ yr}^{-1}. \quad (21)$$

Because our analysis in the previous section is based upon a single column density medium, and each sight line toward the H I region as shown in Fig. 9 will be characterized by a higher H I column density than N_{HI}^0 . Therefore, the contributions to the centre shift from these sightlines will be smaller than that from the sightline for the Strömgren boundary. In order to account for the observed redward shift, we have to lower the column density, which will lead to a lower mass loss rate. However, this result should be taken with much care, noting that the estimate of N_{HI} is highly sensitive to the kinematics between the emission region and the neutral scattering region.

5 DISCUSSION AND OBSERVATIONAL RAMIFICATIONS

The inaccuracy of the estimation of N_{HI} can be attributed to a number of assumptions adopted in this work. The first assumption is that the scattering region is static with respect to the emission region. It is very plausible that the neutral region around the giant component takes the form of the slow stellar wind with a typical velocity of 10 km s $^{-1}$. The amount of center shift 0.64 Å in the Raman scattered He II λ 4850 may also be obtained from the receding velocity $v = 7.9$ km s $^{-1}$ of the scattering region with respect to the emission region. This velocity scale is smaller than the slow stellar wind velocity, and hence our conclusion may be significantly affected. This is much more serious in the case of RR Tel, for which a smaller wavelength shift is concerned.

However, it is also expected that the neutral region possesses both receding and approaching motions that will compensate the kinematic effect to some degree. A more refined

analysis will be possible if we can secure other Raman features including He II λ 4340 formed blueward of H γ , because the amounts of the centre shifts will differ if the effect is due to atomic physics. Currently, it is not feasible to determine the center location of this feature in our spectra. Spectra with longer exposures will be useful in establishing a consistent model.

The assumption that the scattering region is characterized by a single column density may not be valid. A more realistic picture would be a system consisting of spherical shells with density decreasing as r^{-2} , where r is the distance from the centre of the giant. However, the Strömgren boundary due to the strong UV radiation from the white dwarf region complicates this simple picture. Therefore, a more realistic model should be obtained by combining photoionization calculations that should also yield correct emission line ratios (e.g. Mürset & Nussbaumer 1994).

The measurement of the centre shift provides an upper limit of the mass loss rate with the assumption that the scattering region is static with respect to the He II emission region. On the other hand, Lee et al. (2003) provided a rough estimate of the lower bound $\dot{M} = 3 \times 10^{-7} M_\odot \text{ yr}^{-1}$ for the mass loss rate by equating N_{HI} of the sightline for the Strömgren boundary with the column density corresponding to the unit Raman optical depth. We tentatively conclude that the true mass loss rate may be found between the lower and upper bounds found by JL04 and the current work.

When van Groningen (1993) reported the discovery of the Raman scattered He II λ 4850 feature in his spectrum of the symbiotic nova RR Tel, he also noted that it exhibits a similar redward centre shift by an amount $\Delta v = 12$ km s $^{-1}$ in the parent velocity scale. He attributed this centre shift to a relatively receding motion between the emission region and the scattering region. He adopted the atomic data different from ours, where the line center of He II λ 972 appears at 972.09 Å in his analysis.

If we interpret his result using the atomic data adopted in this paper, the redward centre shift of the Raman scattered He II λ 4850 in RR Tel amounts to $\Delta\lambda = 0.33$ Å, a significantly smaller than the value $\Delta\lambda \simeq 1$ Å he quoted. If the scattering region in RR Tel is static with respect to the He II emission region, this redward shift indicates the H I column density $N_{HI} \simeq 4 \times 10^{21}$ Å, which is considerably higher than that in V1016 Cyg. This example shows that the analysis of Raman scattered features requires extremely accurate atomic data and that Raman features can be a very sensitive probe of the density structure around the giant component in symbiotic stars.

ACKNOWLEDGMENTS

We are very grateful to Kang Min Kim and the staffs responsible for BOES of BOAO. We also thank the referee, Hans Martin Schmid, who provided helpful comments that improved the presentation of this paper. This work is a result of research activities of the Astrophysical Research Center for the Structure and Evolution of the Cosmos (ARCSEC) funded by the Korea Science and Engineering Foundation.

REFERENCES

- Arrieta, A. & Torres-Peimbert, S., 2003, ApJS, 147, 97
Bethe, H. A. & Salpeter, E. E., 1957, Quantum Mechanics of One and Two Electron Atoms, Academic Press, New York
Birriel, J., 2003, AAS, 202, 3203
Birriel, J., Espey, B. R., & Schulte-Ladbeck, R. E., 1998, ApJ, 507, 75
Birriel, J., Espey, B. R., & Schulte-Ladbeck, R. E., 2000, ApJ, 545, 1020
Brocksopp, C., Bode, M. F., Eyres, S. P. S., Crocker, M. M., Davis, R., Taylor, A. R., 2002, ApJ, 571, 947
Harries, T. J., & Howarth, I. D. 1996, A&AS, 119, 61
Jung, Y. -C., & Lee, H. -W., 2004, MNRAS, 350, 580
Kenyon, S. J., 1986, The Symbiotic Stars (Cambridge: Cambridge Univ. Press)
Karzas, W. J. & Latter, R., 1961, ApJS, 6, 167
Lee, H. -W., 2003, ApJ, 594, 637
Lee, H. -W., 2000, ApJ, 541, L25
Lee, H. -W., & Hyung, S. 2000, ApJ, 530, 49L
Lee, H. -W., & Lee, K. W. 1997, MNRAS, 287, 211
Lee, H. -W., Kang, Y. W., Byun, Y. I., 2001, ApJ, 551, L121
Lee, H. -W., Sohn, Y.-J., Kang, Y. W., & Kim, H.-I., 2003, ApJ, 598, 553
Mürset, U. & Nussbaumer, H., 1994, A&A, 282, 586
Nussbaumer, H., Schmid, H. M. & Vogel, M., 1989, A&A, 221, L27
Péquignot, D., Baluteau, J.-P., Morisset, C., Boisson, C., 1997, A&Ap, 323, 217
Sadeghpour, H. R., & Dalgarno, A., 1992, J. Phys. B: At. Mol. Opt. Phys., 25, 4801
Saslow, W. M., & Mills, D. L., 1969, Physical Review, 187, 1025
Schmid, H. M. & Schild, H., 1994, A&A, 281, 145
Schmid, H. M. 1995, MNRAS, 275, 227
Schmid, H. M., Schild, H., 2002, A&A, 395, 117
Schmid, H. M. et al., 1999, A&A, 348, 950
Taylor, A. R. & Seaquist, E. R., 1984, ApJ, 286, 263
Van Groningen, E., 1993, MNRAS, 264, 975